

# Electronic Transport and Fermi Surface Topology of Zintl phase Dirac Semimetal $\text{SrZn}_2\text{Ge}_2$

M. K. Hooda<sup>1</sup>, A. Chakraborty<sup>1,2</sup>, S. Roy<sup>3</sup>, A. Agarwal<sup>1</sup>, P. Mandal<sup>4</sup>, S. N. Sarangi<sup>5</sup>, D. Samal<sup>5,6</sup>, V. P. S. Awana<sup>7</sup>, and Z. Hossain<sup>1</sup>

<sup>1</sup> Department of Physics, Indian Institute of Technology, Kanpur-208016, India

<sup>2</sup> Institute of Physics, Johannes Gutenberg Universität, Staudinger Weg 7, 55128 Mainz, Germany

<sup>3</sup> Vidyasagar Metropolitan College, 39, Sankar Ghosh Lane, Kolkata 700006, India

<sup>4</sup> Department of Condensed Matter and Material Physics, S. N. Bose National Centre for Basic Sciences, Block JD, Sector III, Salt Lake, Kolkata 700106, India

<sup>5</sup> Institute of Physics, Bhubaneswar, Bhubaneswar-751005, India

<sup>6</sup> Homi Bhabha National Institute, Anushakti Nagar, Mumbai 400085, India

<sup>7</sup> CSIR National Physical Laboratory, New Delhi, 110012, India

We report a comprehensive study on the electronic transport properties of  $\text{SrZn}_2\text{Ge}_2$  single crystals. The in-plane electrical resistivity of the compound exhibits linear temperature dependence for  $80 \text{ K} < T < 300 \text{ K}$ , and  $T^2$  dependence below  $40 \text{ K}$ , consistent with the Fermi liquid behavior. Both the transverse and longitudinal magnetoresistance exhibit a crossover at critical field  $B^*$  from weak-field quadratic-like to high-field unsaturated linear field dependence at low temperatures ( $T \leq 50 \text{ K}$ ). Different interpretations of this magnetoresistance crossover behavior are presented based on the quantum limit of Dirac Fermions and the specific topology of the Fermi surface of the compound. Abrikosov's theory is employed to explain linear behavior of magnetoresistance at low temperatures. The Hall resistivity data establish  $\text{SrZn}_2\text{Ge}_2$  as a multiband system with contributions from both the electrons and holes. The Hall coefficient is observed to decrease with increasing temperature and magnetic field, changing its sign from positive to negative. The negative Hall coefficient observed at low temperatures in high fields and at high temperatures over the entire field range suggests that the highly mobile electron charge carriers dominate the electronic transport. Our first-principles calculations show that nontrivial topological surface states exist in  $\text{SrZn}_2\text{Ge}_2$  within the bulk gap along the  $\Gamma$ -M path. Notably, these surface states extend from the valence to conduction band with their number varying based on the Sr and Ge termination plane. The Fermi surface of the compound exhibits a distinct tetragonal petal-like structure, with one open and several closed surfaces. Overall, these findings offer crucial insights into the mechanisms underlying the electronic transport of the compound.

## 1. Introduction

Zintl phase compounds are well known for their exceptional thermoelectric properties, and structural stability over a wide range of temperatures [1,2]. Among them, the  $\text{AM}_2\text{X}_2$  family ( $\text{A}$  = Alkali, alkaline-earth, and rare-earth elements;  $\text{M}$  = transition metal;  $\text{X}$  = group 13-16 elements) has drawn significant attention because of their several interesting properties, such as superconductivity (SC), colossal magnetoresistance (MR), metamagnetism, spin density wave, and topological phases such as field-induced topological Hall effect [3-13]. Interestingly, SC was commonly observed for compounds crystallizing in tetragonal  $\text{ThCr}_2\text{Si}_2$ -type structure (space group  $I4/mmm$ ) [3-7]. For example, fully gapped  $s$ -wave SC was observed in  $\text{SrPd}_2\text{Ge}_2$  at  $T_c \sim 2.70 \text{ K}$  [6]. SC found in  $\text{AFe}_2\text{As}_2$  ( $\text{A} = \text{K}, \text{Cs}, \text{Rb}$ ) compounds exhibits a highly unconventional nature [4,5,11]. In case of  $\text{RbFe}_2\text{As}_2$ , SC occurs in the nematic phase [5], whereas, in  $\text{KFe}_2\text{As}_2$ , superconducting order parameter has a complex multi-gap structure [11]. Notably, the former is determined by hole Fermi surfaces and can switch from being nodeless to having octet line nodes depending upon the location of Fermi surfaces within the Brillouin zones [11]. Multiple topological phases have been found in the magnetic  $\text{AM}_2\text{X}_2$  family of compounds through experimental and theoretical investigations [12-17]. Density functional theory calculations revealed a single pair of Weyl nodes in  $\text{EuCd}_2\text{As}_2$ , which could be tuned by changing the canting angle [16]. Magnetotransport measurements further found the anomalous Hall effect and negative longitudinal MR,

indicative of a chiral anomaly, supporting the Weyl node picture in  $\text{EuCd}_2\text{As}_2$  [16]. The application of high magnetic fields was observed to suppress A-type antiferromagnetic ordering in isostructural  $\text{EuZn}_2\text{As}_2$ , giving rise to large negative in-plane MR [17]. Like  $\text{EuCd}_2\text{As}_2$ ,  $\text{EuZn}_2\text{As}_2$  was also reported to exhibit the nonlinear anomalous Hall effect but of a smaller magnitude due to relatively weak spin-orbit coupling (SOC) [17]. The existence of massless 2D Dirac fermions was confirmed in the antiferromagnetic compounds  $\text{BaFe}_2\text{As}_2$  and  $\text{SrFe}_2\text{As}_2$  through the field-dependent infrared studies and theoretical calculations [12].

In comparison to their magnetic counterparts, the nonmagnetic Zintl phase  $\text{AM}_2\text{X}_2$  family of topological phases has received the least attention. Recent theoretical investigations of alkaline-earth based Zintl phases have predicted a plethora of new topological candidate materials, such as  $\text{SrIn}_2\text{As}_2$  (dual topological insulator),  $\text{A}(\text{Ca}, \text{Sr}, \text{Ba})\text{Cd}_2\text{As}_2$  (Dirac semimetals under pressure),  $\text{CaZn}_2\text{Bi}_2$ , and  $\text{CaCd}_2\text{Bi}_2$  (topological crystalline insulators) [15,18-20]. The experimental authentication of topological phases in the case of nonmagnetic Zintl phases is realized only in a limited number of materials.  $\text{SrAl}_2\text{Si}_2$  and  $\text{CaAl}_2\text{Si}_2$  present a good examples of it, where nontrivial topology was confirmed from the Landau level fan diagram obtained through the Shubnikov-de Hass oscillations experiment [9,21].

Motivated by the remarkable potential of 122 family compounds to explore the topological physics and exotic electronic transport properties, which are primarily governed by their distinctive

Fermi surface topology [5,11,12,21,22], our investigation focuses on a nonmagnetic Zintl phase material,  $\text{SrZn}_2\text{Ge}_2$ , from this family. The crystal structure and synthesis of polycrystalline  $\text{SrZn}_2\text{Ge}_2$  are already reported in the literature [23]. Moreover, a study on the electronic structure and the physical properties of  $\text{SrZn}_2\text{Ge}_2$  is absent in the literature.

In this paper, we report the electronic transport properties of single-crystalline  $\text{SrZn}_2\text{Ge}_2$  by means of MR, Hall resistivity measurements, and electronic band structure calculations. We discuss the features of the electronic transport data in the context of conventional charge carriers, Dirac fermions, and the Fermi surface topology of the compound. Our study unveils the nontrivial topology and exotic transport properties of  $\text{SrZn}_2\text{Ge}_2$  such as linear transverse and longitudinal MR, field- and temperature-induced sign reversal of the Hall coefficient.

## 2. Experimental details and methods

Single crystals of  $\text{SrZn}_2\text{Ge}_2$  were prepared using Pb-flux reactions. The first batch of crystals was grown with the stoichiometric ratio  $\text{Sr}:\text{Zn}:\text{Ge}:\text{Pb} = 1:1:1:3$ . We also tried other stoichiometric compositions, such as 1:2:2:5, 1:2:2:7, and 1:2:2:10. Each approach yielded very shiny and thin flakes of single crystals. The reactions took place in vacuum-sealed quartz tubes, where the reactants were first loaded into an alumina crucible, and then the crucible was put into a quartz tube. The mixture was heated to 1050 °C in 20 h and maintained at this temperature for 24 h to obtain a homogeneous solution. In the next step, the furnace was slowly cooled to 500 °C at the rate of 3 °C/h, and single crystals were isolated from Pb-flux using centrifuging process. We would further like to mention here that changing the centrifuge temperature from 500 to 650 °C did not affect the quality of crystals.

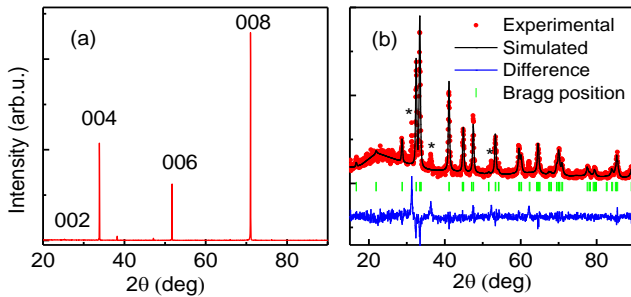


**Fig. 1.** X-ray diffraction pattern of  $\text{SrZn}_2\text{Ge}_2$  (a) Single crystal. (b) Powder. The marked peaks in the diffraction pattern are due to Pb-flux.

The X-ray diffraction (XRD) pattern obtained from a top surface of a representative  $\text{SrZn}_2\text{Ge}_2$  single crystal is shown in Fig. 1. It shows the crystal growth along (00 $l$ ) plane. The typical size of crystals is up to 3 mm in length, 2 mm in width, and 0.1 mm in thickness. Energy dispersive X-ray spectroscopy measurements carried out on several crystals showed a fairly homogeneous elemental distribution and chemical composition close to the

desired stoichiometry. The Rietveld refinement performed on the powder XRD of several crushed single crystals showed that  $\text{SrZn}_2\text{Ge}_2$  crystallizes in a tetragonal  $\text{ThCr}_2\text{Si}_2$ -type structure with space group  $I4/mmm$  (139). The lattice parameters obtained from the Rietveld refinement are  $a = b = 4.39$  Å, and  $c = 10.632$  Å, which are close to those reported in the literature [23].

Magnetotransport studies were performed in the temperature range of 2-300 K in magnetic fields up to 9 T using the Quantum Design Physical Property Measurement System. The experiments were done employing a standard four-probe technique. The magnetic properties were investigated in the same temperature range using a 7-T Quantum Design SQUID Magnetometer.

## 3. Computational methods

The electronic structure calculations of bulk  $\text{SrZn}_2\text{Ge}_2$ , were performed using the density functional theory (DFT) in the plane wave basis set. We used the Perdew-Burke-Ernzerhof (PBE) [24] implementation of the generalized gradient approximation (GGA) for the exchange-correlation. This was combined with the projector augmented wave potentials [25,26] as implemented in the Vienna ab initio simulation package [27]. GGA calculations were carried out with and without SOC. In the former case, SOC was included as a second variational form to the original Hamiltonian. The kinetic energy cutoff of the plane wave basis set was chosen to be 500 eV. The momentum-space calculations for the Brillouin zone (BZ) integration of bulk were performed on a  $\Gamma$ -centered,  $12 \times 12 \times 6$  k-point grid. To calculate the surface spectral function for finite slab geometry of  $\text{SrZn}_2\text{Ge}_2$ , we construct the tight-binding model Hamiltonian by deploying atom-centered Wannier functions within the VASP2WANNIER90 [28]. Utilizing the obtained tight-binding model, we calculated the surface spectral function using the iterative Green's function method, as implemented in the Wannier Tools package [29].

## 4. Results and discussion

### 4.1. Electronic band structure and Fermi surface topology

Bulk  $\text{SrZn}_2\text{Ge}_2$  crystallizes in the tetragonal  $I4/mmm$  (139) space group and has two-fold ( $C_{2i}$ ) and four-fold ( $C_{4i}$ ) rotational symmetry, inversion, and five mirror symmetries, such as  $m_{001}$ ,  $m_{010}$ ,  $m_{100}$ ,  $m_{110}$ , and  $m_{1-10}$ . Each conventional unit cell of  $\text{SrZn}_2\text{Ge}_2$  consists of two formula units that are inverted with respect to the body center of the cell, as illustrated in Fig. 2(a). The  $\text{ZnGe}_4$  tetrahedra accommodating Zn-Ge nearest neighbor bonds with a bond length of  $\sim 2.59$  Å form an edge-shared network [see Fig. 2(b)] on the crystallographic  $ab$ -plane. The Sr atoms are situated in between the ZnGe planes, which are stacked along the  $c$  axis.

To comprehend the electronic band structure, we start with non-spin polarized calculations while enforcing spin degeneracy. We present the band dispersion along various high-symmetry directions and the density of states (DOS) of  $\text{SrZn}_2\text{Ge}_2$  in Figs. 2(d) and 2(e). The finite contributions of DOS at the Fermi level suggest that the system is metallic. The four bands contributing to the DOS at the Fermi level are marked in green, red, purple,

and cyan. The orbital projected DOS calculations show that the Ge- $p$  states dominate the bands near the  $E_F$ , with Sr- $d$ , Zn- $s$ , and Zn- $p$  states making small but significant contributions. The electronic band structure shows a large hole pocket in the top valence band (red) along the  $\Gamma$ -X path and a small hole pocket at the Z point, which has contributions from the two highest valence bands (shown in red and green).

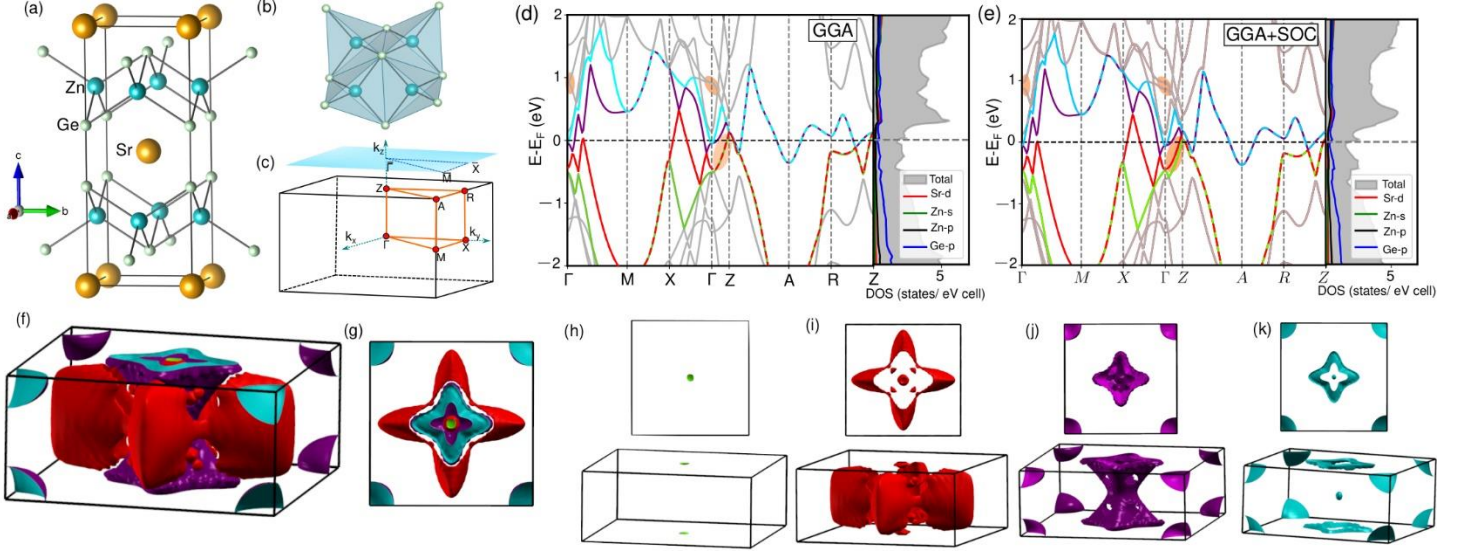


**Fig. 2.** (a) The conventional unit cell containing two formula units of bulk  $\text{SrZn}_2\text{Ge}_2$ . (b) The edge shared local  $\text{ZnGe}_4$  tetrahedral network. (c) The irreducible Brillouin zone (BZ) of the bulk along with (001) projected surface as shown in cyan color. The density of states (grey shaded region) and bulk energy dispersion within (d) GGA and (e) GGA+SOC framework plotted along the high symmetry paths. The orbital decomposed DOS of Sr- $d$  (red), Zn- $s$  (green), Zn- $p$  (black) and Ge- $p$  (blue) suggest dominant contribution of Ge- $p$  state near the Fermi energy. The SOC-induced lifted degeneracy of bands is shown in the orange shaded region. The side (f) and top (g) view of the overall Fermi surface depict a tetragonal petal like feature. The individual Fermi surface contributions of four bands (green, red, purple and cyan) near the Fermi level are presented in (h), (i), (j) and (k), respectively. The Fermi surface of the first conduction band (purple) is an open Fermi surface.

The two lowest conduction bands generate two electron pockets at the A point and between the R-Z path, as shown in Fig. 2(d). Additionally, a very small electron pocket contributed by the first conduction band is observed near the  $\Gamma$  point. The presence of several holes and electron pockets near the  $E_F$  suggests that both types of charge carriers are involved in the transport properties of the compound. To examine the impact of SOC on the low-energy electronic bands, we have also calculated energy dispersion within the GGA+SOC framework, as shown in Fig. 2(e). We find that SOC has a negligible effect on the electronic structure, except for some degeneracy lifting near the  $\Gamma$  point, as shown by the shaded orange region.

Next, we calculated the bulk Fermi surface from the four bands near the Fermi energy. We present the side and top view of the overall bulk Fermi surface of  $\text{SrZn}_2\text{Ge}_2$  in Fig. 2(f) and Fig. 2(g), respectively. The figures exhibit a distinct tetragonal petal-like structure of the Fermi surface. The individual Fermi surfaces for the green, red, purple, and cyan bands are plotted in Figs. 2(h), 2(i), 2(j), and 2(k), respectively. We find closed Fermi surfaces for all the bands except the first conduction band as shown in

purple in Fig. 2(d). The latter is an open Fermi surface with a hyperboloid shape that extends over the adjacent BZ.

#### 4.2. Non-trivial surface states

Our examination of the bulk electronic structure, which have several band crossings near the Fermi level, led us to investigate further the topological nature of the system. The detailed theoretical calculations of the  $Z_2$  topological indices, which are presented in the supplementary information, clearly suggest that  $\text{SrZn}_2\text{Ge}_2$  is strongly topological with a nontrivial  $Z_2$  index (1;111). We further explore the existence of nontrivial surface states in the system. Using the layered stacking crystal structure, we calculated the spectral functions by creating a finite slab geometry along the (001) plane. The resulting bulk and surface spectral functions for Ge and Sr terminations are shown in Fig. 3(a) and 3(b), respectively. We found that along the  $\Gamma$ -X path, the surface states, as marked by green arrows, are deep within the bulk states. Interestingly, along the  $\Gamma$ -M path, there exist non-trivial surface states within the bulk band gap. The surface states extend from the conduction to the valence bands. For Ge and Sr termination, we find one and two surface bands (pointed with

cyan arrows) in the bulk energy gap, respectively. Our findings demonstrate that the number of non-trivial surface states within the gap depends upon the termination plane, a critical aspect in comprehending this system.

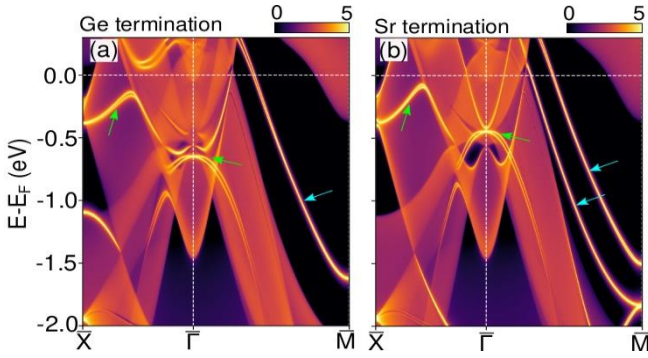


**Fig. 3.** The calculated momentum resolved spectral density plots along the X- $\Gamma$ -M direction, (a) for Ge and (b) for Sr terminations. There exist non-trivial surface states within the bulk band gap along the  $\Gamma$ -M direction. The number of these non-trivial surface states (marked by cyan arrows) crucially depends on the type of the termination.

#### 4.3. Electrical resistivity

Figure 4 presents the temperature ( $T$ ) dependence of zero-field electrical resistivity ( $\rho$ ) measured within the  $ab$ -plane of two  $\text{SrZn}_2\text{Ge}_2$  single crystals (marked by C1 and C2), which were grown in two different batches. Both crystals show very similar behavior of  $\rho(T)$ . At room temperature,  $\rho$  value for crystals, C1 and C2 is around 121 and 76.7  $\mu\Omega$  cm, respectively. These values are comparable to or slightly smaller than those reported for the isostructural compound  $\text{SrPd}_2\text{Ge}_2$  [6]. In the range of 80-300 K,  $\rho$  exhibits an almost linear temperature dependence (as depicted by cyan line in Fig. 4) due to electron-phonon scatterings. Such a linear behavior of  $\rho(T)$  could be explained by the Bloch-Gruneisen (BG) model, which assumes the spherical Fermi surface of metal limited to the first Brillouin zone and phonon spectrum described by Debye temperature. At low temperatures (7.5-40 K), we observe  $\rho \propto T^2$ , a key feature of Fermi-liquid behavior. The least-square fitting to the data by  $\rho(T) = \rho_0 + A_{e-e}T^2$  at low temperatures (7.5-40 K) yields residual resistivity  $\rho_0 \approx 13.8$   $\mu\Omega$  cm and electron-electron scattering coefficient  $A_{e-e} \approx 3.04$  n $\Omega$  cm/K<sup>2</sup>, which is comparable to that of  $\text{BaCo}_2\text{As}_2$  ( $\sim 3.94$  n $\Omega$  cm/K<sup>2</sup>) [30].

At  $\sim 7.2$  K,  $\rho(T)$  shows the sharp superconducting drop, however it is incipient since  $\rho(T)$  does not tend to approach zero value. The applied magnetic field of more than 0.15 T suppresses SC below 2 K, as shown in the top left inset of Fig. 4. The estimated superconducting volume fraction is very small,  $\approx 1.8$  % at 4 K (see top right inset of Fig. 4), suggesting the filamentary character of SC. Possibly, the SC in  $\text{SrZn}_2\text{Ge}_2$  is not an intrinsic feature but rather a result of Pb flux residue [31]. With the application of

magnetic field ( $B \parallel c$ ,  $I \parallel ab$ ),  $\rho$  increases in the low-temperature region (see bottom inset of Fig. 4), however, the relative increase is rather slow in comparison to that reported for various 122 phase topological semimetals [9,17,21].

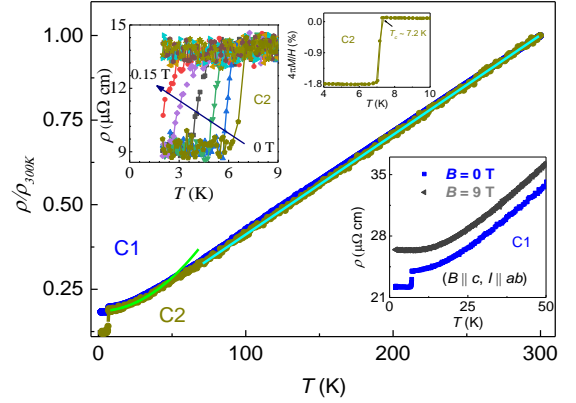


**Fig. 4.** The temperature dependence of normalized in-plane electrical resistivity of  $\text{SrZn}_2\text{Ge}_2$  crystals denoted by C1 and C2 at zero field for current applied within the  $ab$ -plane. The green and cyan lines represent the quadratic and linear fits to the data respectively as described in the text. Top inset (left): the field-dependence of electrical resistivity in the superconducting region when the field is applied along the  $c$  axis of the crystal and perpendicular to the current direction. Top inset (right): magnetic susceptibility in the vicinity of the superconducting transition at  $H = 10$  Oe, representing the superconducting volume fraction. The bottom inset shows the electrical resistivity under applied fields of 0 and 9 T when  $B \parallel c$ , and  $I \parallel ab$ .

#### 4.4. Magnetoresistance

Figures 5(a) and 5(b) present the transverse and longitudinal MR measured at various temperatures for field configurations  $B \parallel c$  and  $B \parallel ab$  respectively with current  $I$  flowing in the  $ab$ -plane. The MR is positive and monotonically increases with the field without any sign of saturation. However, the value of transverse (longitudinal) MR is small, just about 7% (5%) at 10 K and 9 T for  $B \parallel c$  ( $B \parallel ab$ ). Moreover, this value is larger than the typically reported values of 0.8 – 3 % for isostructural compounds like  $\text{SrPd}_2\text{Ge}_2$  and  $\text{BaNi}_2\text{P}_2$  [32,33]. MR continuously decreases with increasing temperature and becomes less than 1 % at 300 K. At low temperatures ( $T \leq 50$  K), MR for both field configurations is primarily governed by the linear field-dependence term, accompanied by a small quadratic term ( $\text{MR} = aB + O(B^2)$ ) in the high-field region, which reduces to a quadratic-like response in the low-field region. This type of crossover behavior has been reported in several Dirac materials [34-39]. To further confirm the existence of a linear MR component in data, we performed a power law fit ( $\text{MR} \propto B^m$ ) across a broad field range of 2-9 T (see supplementary Fig. S2). At higher temperatures ( $T \geq 200$  K), the fitting yields the value of exponent,  $m = 2$  (Fig. 5(c)). Remarkably, the latter decreases consistently with decreasing temperature, eventually approaching value of  $\sim 1.35$  at 2 K. These



findings clearly demonstrate that linear MR is the dominant term at low temperatures and higher fields.

The transition from quadratic field dependence of MR in the low-field regime to linear field dependence of MR in the high-field regime could be understood by considering the crossover (at a certain critical field strength  $B^*$ ) between the semiclassical and quantum transport regimes. According to Abrikosov, the quantum limit could be achieved if all the carriers occupy the lowest Landau level (LL) and splitting between LLs ( $\Delta_{LL}$ ) is larger than the Fermi energy  $E_F$  of the system and inaccessible to the thermal fluctuations ( $k_B T$ ) [40]. In the case of parabolic dispersive bands, the condition  $\Delta_{LL} > k_B T$  is very difficult to achieve due to very high field requirements, as  $\Delta_{LL}$  is directly proportional to  $B$  ( $\Delta_{LL} = \hbar e B / m^*$ ). However, in the case of Dirac fermions, the above-described condition could be achieved at moderate field strengths because of the square root  $B$ -dependence of  $\Delta_{LL}$  ( $= \pm v_F \sqrt{2e\hbar B}$ ). Although we do not reach the absolute quantum limit up to the field strength of 9 T (as evident from the absence of Shubnikov de Haas oscillations), but even at this field strength, linear quantum MR could be observed with more than one LL filled [34]. At low temperatures, where thermal fluctuations effects become weaker, the linear component of MR at higher fields becomes even more pronounced (see inset of Fig. 5(a)). It clearly suggests that the system tends to approach the quantum limit with decreasing temperature.

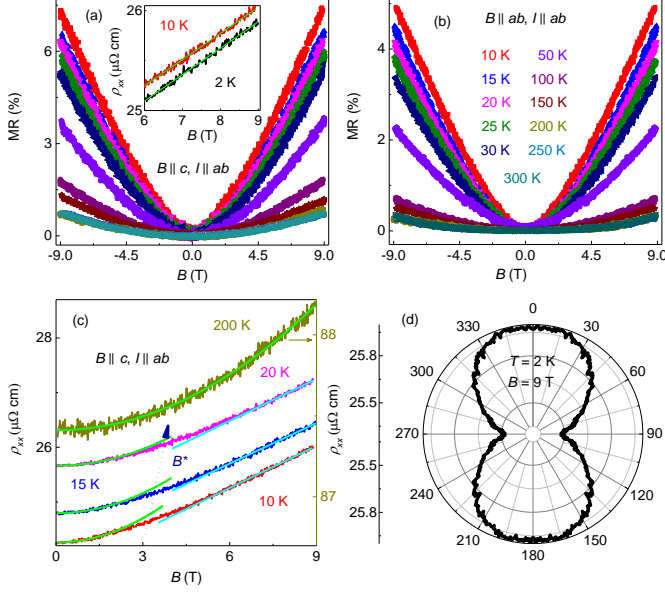


**Fig. 5.** Magnetoresistance isotherms of single-crystalline  $\text{SrZn}_2\text{Ge}_2$  measured within the  $ab$ -plane (a) when the field is applied along the  $c$ -axis and (b) along the  $ab$ -plane. Inset in (a) shows the linear behavior of magnetoresistivity at temperatures of 2 and 10 K as a function of the field. (c) The transverse resistivity ( $B \parallel c, I \parallel ab$ ) as a function of field  $B$  at a few selected temperatures of 10, 15, 20 and 200 K. The green and cyan lines are quadratic and linear fits to the data respectively. The dashed line arrow illustrates the critical field  $B^*$  that marks the boundary between the onset of quadratic and linear behavior of magnetoresistance. (d) Polar representation of the angular dependence of resistivity measured at  $B = 9$  T and  $T = 2$  K.  $\theta$  is the angle defined between the magnetic field and the  $c$ -axis of the crystal.

Further, we estimate the critical field  $B^*$  (see Fig. 5(c)) from magnetoresistivity curves below 50 K and fit the data using equation  $B^*(T) = \frac{1}{2e\hbar v_F^2} (E_F + k_B T)^2$ , which is defined in the quantum limit of Dirac fermions. The last term of the equation defines the LL splitting ( $\Delta_{LL} = E_F + k_B T$ ). Our fitting results yield the values of the Fermi velocity  $v_F \approx 1.53 \times 10^5$  m/s and the Fermi energy  $E_F \approx 8.97$  meV. The  $v_F$  value is comparable to that reported for isostructural compounds such as  $\text{BaFe}_2\text{As}_2$  and  $\text{SrMnBi}_2$  [35, 38]. The electronic band structure calculations of  $\text{SrZn}_2\text{Ge}_2$  show the existence of multiple Dirac bulk and surface states in the vicinity of the Fermi level (see Figs. 2(d), 2(e) and Fig. 3). These states coexist with multiple conventional electron and hole pockets. The linear MR observed in our experimental data could be attributed to bulk and non-trivial surface states crossing the Fermi level (see Fig. 3).

Furthermore, we would like to mention the other possible mechanisms of linear MR reported in the literature. One such mechanism is the formation of open orbits in the Fermi surface [41]. The open orbit is present in the hyperboloid-shaped Fermi surface of the compound (shown in the purple color in Fig. 2(j)). Nevertheless, it cannot explain linear MR for  $B \parallel c$ , where the magnetic field vector scans the closed Fermi surfaces in a plane normal to them. It may, however contribute to the linear MR observed for  $B \parallel ab$ . Nonetheless, the linear MR cannot be solely attributed to this mechanism because the topological bulk and surface states near the Fermi level also play a role in contributing to the linear MR.

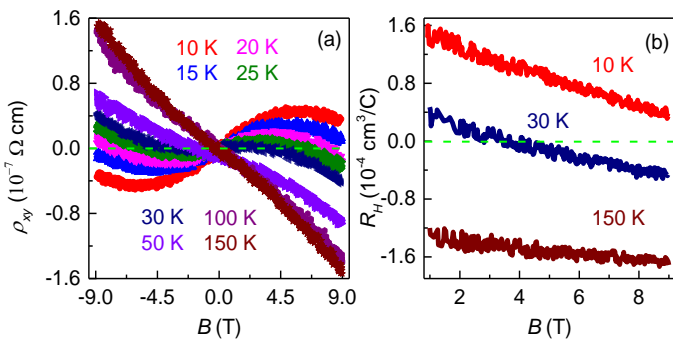
Hinlopen *et al.* [42] recently proposed a specific model for linear to quadratic field dependence of MR in a wide range of materials. The key postulate of this specific model is impeded cyclotron motion on the Fermi surface, which can result in linear- $B$  to quadratic crossover behavior [42]. Such an impeded cyclotron motion can occur, for example, due to the Fermi surface sectors, partially gapped Fermi surfaces, van Hove singularities, etc. [42]. Given that this model is applicable to multiband systems with any arbitrary shape of Fermi surface and that  $\text{SrZn}_2\text{Ge}_2$  has multiple boundaries on the Fermi surface, it could possibly explain the MR trend in our data. The Fermi surface topology of  $\text{SrZn}_2\text{Ge}_2$  is shown in the section A (see Figs. 2(f)-(k)), where the negative curvatures of dominating tetragonal, four-fold shaped Fermi surfaces are evident in moving from one vertex to another. It could result in alternating Fermi surface sectors with electron- and hole-like characters. However, some caution must be exercised in pursuing this model despite the supportive features of Fermi surface topology of the compound. This model for isotropic 2D Fermi surface with tetragonal symmetry predicts linear or quasi-linear magnetoresistivity and quasi-linear Hall resistivity in low magnetic fields, which seems consistent with our data. However, at very high fields, it predicts strictly linear Hall resistivity independent of carriers' mass and relaxation time [42]. It strongly differs from our Hall resistivity data, which exhibits strong nonlinear field dependence at higher fields (see

Fig. 6). Although, it should be noted that the maximum field applied in our data could be of intermediate strength as we do not observe the quantum oscillations at this field strength.

In Fig. 5(d), we show the symmetrized polar curve of angle-dependent magnetoresistivity at 2 K and 9 T. In performing the experiment, the current was confined within the *ab*-plane of the crystal, while the magnetic field was rotated from out of plane (*c*-axis) to the in-plane direction (*ab*-plane). The dumbbell-like pattern of magnetoresistivity traces the two-fold symmetry and indicates the anisotropic Fermi surface of SrZn<sub>2</sub>Ge<sub>2</sub>. The maximum of resistivity occurs at  $\theta = 0^\circ, 180^\circ$  ( $B \parallel c$ ) while minimum at  $\theta = 90^\circ, 270^\circ$  ( $B \parallel ab$ ). However, the overall change in angular resistivity is very small, suggesting a very small anisotropic factor, which reflects the 3D electronic transport in the compound.

#### 4.5. Hall resistivity

Next, we discuss the field dependence of Hall resistivity ( $\rho_{xy}$ ), which is shown in Fig. 6(a). At low temperatures ( $T \leq 20$  K), the  $\rho_{xy}$  is positive, indicating that the holes dominate transport in the compound. Further, the  $\rho_{xy}$  behavior shifts from nearly linear at low fields to nonlinear at high fields. The maximum in  $\rho_{xy}$  is observed at higher fields, which, for example, appears around 5 T for 10 K data. It gradually shifts to lower fields and is suppressed as the temperature rises. Above 30 K,  $\rho_{xy}$  becomes negative across the entire field range. Remarkably, the nonlinear behavior of  $\rho_{xy}$  persists up to the highest measured temperature of 150 K. This is consistent with the multiband transport picture predicted by the presence of various electron and hole pockets at the Fermi level, as shown in the electronic band structure of the compound in Figs. 2(d) and 2(e).



**Fig. 6.** (a) Hall resistivity of single-crystalline SrZn<sub>2</sub>Ge<sub>2</sub> as a function of the magnetic field measured in the temperature range 10–150 K. The current is applied along *ab* – plane and the magnetic field is applied along *c*-axis of crystal. (b) The field dependence of Hall coefficients at a few selected temperatures of 10, 30, and 150 K. The low-field data points are omitted for clarity.

In the literature, for quantitative analysis of nonlinear  $\rho_{xy}$ , usually, a two-band model is employed. This model is suitable for multiband systems with a more or less spherical Fermi surfaces and constant and isotropic relaxation times within the bands [43]. In the case of SrZn<sub>2</sub>Ge<sub>2</sub>, the Fermi surface is quite complex and

strongly deviates from the spherical Fermi surface. The isotropic relaxation time approximation is also unlikely to hold due to the very anisotropic Fermi surface. Therefore, we have calculated the Hall coefficient  $R_H \approx 1.49 \times 10^{-4} \text{ cm}^3/\text{C}$  at 10 K from the low-field region ( $B < 2$  T). This value is comparable to those reported in other isostructural compounds, such as SrPd<sub>2</sub>Ge<sub>2</sub> and BaNi<sub>2</sub>P<sub>2</sub> [32,33]. Although, one noted difference of these compounds with SrZn<sub>2</sub>Ge<sub>2</sub> is that they show electron carriers predominance in low temperatures.

Furthermore, we present a qualitative discussion of  $\rho_{xy}$ . The appearance of maximum at higher fields and negative  $\rho_{xy}$  at low temperatures, which indicates carrier switching from holes to electrons, could be understood by considering the different temperatures and field-dependences of the average mobilities of electrons ( $\mu_e$ ) and holes ( $\mu_h$ ), with the former ones being more mobile. As the temperature increases, both  $\mu_h$  and  $\mu_e$  decrease, but  $\mu_e$  remains relatively larger than  $\mu_h$ . This results in a negative  $R_H$  despite the compound having a comparatively higher carrier density of holes than electrons near the Fermi level. The variation of  $R_H$  with magnetic field and temperature (Figs. 6(a) and (b)) clearly indicates the role of Fermi surface's specific shape and geometry in the electronic transport. The in-plane view of the Fermi surface is presented in Fig. 2(g)), which shows several ovals- and tetragonal-shaped Fermi surfaces, with the latter having positive and negative curvatures of different arc lengths. It is possibly the local curvatures of the latter Fermi surfaces that give rise to anisotropy in effective masses of carriers. These Fermi surfaces mainly contribute to MR and  $\rho_{xy}$  as the area of oval-shaped Fermi surfaces is very small. High mobility of electrons may occur due to relatively smaller effective masses and longer relaxation times of electrons than holes. The Dirac fermions could account for some of these relatively high-mobility electrons. The contribution of Dirac fermions is also evident from low-temperature MR behavior at higher fields and the presence of bulk and nontrivial surface states near the Fermi level in the electronic band structure of the compound (see Figs. 2 and 3).

Moreover, to elucidate the sign change in  $R_H$  under an applied field and temperature, we refer to the semiclassical model developed by N. P. Ong for weak field limits ( $\omega\tau < 1$ ) in 2D metals [44]. This model has been generalized for 3D systems and can be employed for multiband systems such as SrZn<sub>2</sub>Ge<sub>2</sub> [44]. According to this model,  $\rho_{xy}$  (or  $\sigma_{xy}$ ) is determined by the Stokes area  $A_l [= \oint dl(k) \times l(k)]$  swept out by the vector  $l(k)$  ( $= v_k \tau k$ ). The circulation of vector  $l(k)$  is directly related to the local curvature of the Fermi surface. When the circulation of  $l(k)$  is different in different regions,  $\rho_{xy}$  (or  $\sigma_{xy}$ ) changes sign. In SrZn<sub>2</sub>Ge<sub>2</sub>, the dominant Fermi surface has a four-fold symmetry and comprises segments of large curvature sandwiched between the segments of small curvature. This geometry is ideal for generating different circulations of  $l(k)$ , leading to the sign change in  $R_H$ .

## 5. Conclusions

In summary, we presented detailed electronic transport properties of single-crystalline  $\text{SrZn}_2\text{Ge}_2$ . The electrical resistivity measured in the  $ab$ -plane shows  $T^2$  dependence below 40 K, and linear behavior above 80 K. The transverse and longitudinal magnetoresistance exhibit a crossover from  $B^2$  dependence in weak fields to linear- $B$  dependence in high fields at low temperatures ( $T \leq 50$  K). Several topological bulk and surface states near the Fermi level, including non-trivial surface states, as evident from the electronic band structure calculations, provide evidence for the existence of Dirac fermions in  $\text{SrZn}_2\text{Ge}_2$ . The overall behavior of the observed magnetoresistance is understood within the framework of Abrikosov's theory of Landau levels in the quantum limit of Dirac fermions and the tetragonal-shaped Fermi surface topology of the compound. Analysis of the temperature and field dependence of Hall resistivity, including its sign change from positive to negative at higher fields and temperatures, suggests that high mobility electron charge carriers dominate the electronic transport properties of  $\text{SrZn}_2\text{Ge}_2$  despite the compound being a multiband system with multiple electron and hole pockets, as revealed by the Hall resistivity data and electronic band structure calculations.

## Acknowledgements

Z. H. acknowledges Indian Institute of Technology (IIT) Kanpur and the Department of Science and Technology (DST), India, [Grant No. DST/NM/TUE/QM06/2019 (G)] for financial support. A. C. acknowledges IIT Kanpur, and the Science and Engineering Research Board (SERB) National Postdoctoral Fellowship (PDF/2021/000346), India for financial support. A. C. and A. A. thank CC-IITK for providing the High-Performance Computing facility. P. M. acknowledges the use of Technical Research Centre (TRC) instrument facilities of S. N. Bose National Centre for Basic Sciences, India and the technical assistance of Dr. M. Roy during the measurements.

## References

- [1] W. Peng, S. Chanakian and A. Zevalkink, *Inorg. Chem. Front.* **5** (2018) 1744.
- [2] S. M. Kauzlarich, A. Zevalkink, E. Toberer, and G. J. Snyder, Chapter 1 Zintl phases: Recent developments in thermoelectrics and future outlook, *Thermoelectric Materials and Devices*, The Royal Society of Chemistry, London, 2017.
- [3] M. Rotter, M. Tegel, and D. Johrendt, *Phys. Rev. Lett.* **101** (2008) 107006.
- [4] K. Sasmal, B. Lv, B. Lorenz, A. M. Guloy, F. Chen, Y.-Y. Xue, and C.-W. Chu, *Phys. Rev. Lett.* **101** (2008) 107007.
- [5] X. Liu, R. Tao, M. Ren, W. Chen, Q. Yao, T. Wolf, Y. Yan, T. Zhang, and D. Feng, *Nat. Commun.* **10** (2019) 1039.
- [6] N. H. Sung, J.-S. Rhyee, and B. K. Cho, *Phys. Rev. B* **83** (2011) 094511.
- [7] C. W. Chen, C. H. Huang, Y. B. You, M. F. Tai, Y. Y. Hsu, and H. C. Ku, *JPS Conf. Proc.* **3** (2014) 015036.
- [8] A. M. Goforth, P. Klavins, J. C. Fetting, and S. M. Kauzlarich, *Inorg. Chem.* **47** (2008) 11048.
- [9] S. Malick, A. B. Sarkar, A. Laha, M. Anas, V. K. Malik, A. Agarwal, Z. Hossain, and J. Nayak, *Physical Rev. B* **106** (2022) 075105.
- [10] T. Berry, S. R. Parkin, and T. M. McQueen, *Phys. Rev. Mater.* **5** (2021) 114401.
- [11] K. Okazaki, Y. Ota, Y. Kotani, W. Malaeb, Y. Ishida, T. Shimojima, T. Kiss, S. Watanabe, C.-T. Chen, K. Kihou, C. H. Lee, A. Iyo, H. Eisaki, T. Saito, H. Fukazawa, Y. Kohori, K. Hashimoto, T. Shibauchi, Y. Matsuda, H. Ikeda, H. Miyahara, R. Arita, A. Chainani, and S. Shin, *Science* **337** (2012) 1314.
- [12] Z.-G. Chen, L. Wang, Y. Song, X. Lu, H. Luo, C. Zhang, P. Dai, Z. Yin, K. Haule, and G. Kotliar, *Phys. Rev. Lett.* **119** (2017) 096401.
- [13] J. Yan, Z. Z. Jiang, R. C. Xiao, W. J. Lu, W. H. Song, X. B. Zhu, X. Luo, Y. P. Sun, and M. Yamashita, *Phys. Rev. Research* **4** (2022) 013163.
- [14] X. Gui, I. Pletikoscic, H. Cao, H.-Ju Tien, X. Xu, R. Zhong, G. Wang, T.-R. Chang, S. Jia, T. Valla, W. Xie, and R. J. Cava, *ACS Cent. Sci.* **5** (2019) 900.
- [15] A. B. Sarkar, S. Mardanya, S.-M. Huang, B. Ghosh, C.-Yi Huang, H. Lin, A. Bansil, T.-R. Chang, A. Agarwal, and B. Singh, *Phys. Rev. Mater.* **6** (2022) 044204.
- [16] K. M. Taddei, L. Yin, L. D. Sanjeewa, Y. Li, J. Xing, C. dela Cruz, D. Phelan, A. S. Sefat, and D. S. Parker, *Phys. Rev. B* **105** (2022) L140401.
- [17] Z.-C. Wang, E. Been, J. Gaudet, G. M. A. Alqasseri, K. Fruhling, X. Yao, U. Stuhr, Q. Zhu, Z. Ren, Y. Cui, C. Jia, B. Moritz, S. Chowdhury, T. Devereaux, and F. Tafti, *Phys. Rev. B* **105** (2022) 165122.
- [18] L.-Y. Feng, R. A. B. Villaos, A. B. Maghirang III, Z.-Q. Huang, C.-H. Hsu, H. Lin, and F.-C. Chuang, *Sci. Rep.* **12** (2022) 4582.
- [19] M. N. R. Perez, R. A. B. Villaos, L.-Y. Feng, A. B. Maghirang III, C.-P. Cheng, Z.-Q. Huang, C.-H. Hsu, A. Bansil, and F.-C. Chuang, *Appl. Phys. Rev.* **9** (2022) 011410.
- [20] J. M. DeStefano and L.-L. Wang, *Phys. Rev. B* **103** (2021) 115207.
- [21] H. Su, X. Shi, W. Xia, H. Wang, X. Hanli, Z. Yu, X. Wang, Z. Zou, N. Yu, W. Zhao, G. Xu, and Y. Guo, *Phys. Rev. B* **101** (2020) 205138.
- [22] I. R. Shein and A. L. Ivanovskii, *Phys. Rev. B* **83** (2011) 104501.
- [23] V. V. Romaka, M. Falmbigl, A. Grytsiv, and P. Rogl, *J. Solid State Chem.* **186** (2012) 87.
- [24] J. P. Perdew, K. Burke, and M. Ernzerhof, *Phys. Rev. Lett.* **77** (1996) 3865.
- [25] P. E. Blöchl, *Phys. Rev. B* **50** (1994) 17953.
- [26] G. Kresse and D. Joubert, *Phys. Rev. B* **59** (1999) 1758.
- [27] G. Kresse and J. Furthmüller, *Phys. Rev. B* **54** (1996) 11169.

- [28] N. Marzari, and D. Vanderbilt, Phys. Rev. B **56** (1997) 12847.
- [29] Q.-S. Wu, S.-N. Zhang, H.-F. Song, M. Troyer, and A. A. Soluyanov, Comput. Phys. Commun. **224** (2018) 405.
- [30] V. K. Anand, D. G. Quirinale, Y. Lee, B. N. Harmon, Y. Furukawa, V. V. Ogloblichev, A. Huq, D. L. Abernathy, P. W. Stephens, R. J. McQueeney, A. Kreyssig, A. I. Goldman, and D. C. Johnston, Phys. Rev. B **90** (2014) 064517.
- [31] B. T. Matthias, T. H. Geballe, and V. B. Compton, Rev. Mod. Phys. **35** (1963) 1.
- [32] N. H. Sung, Y. J. Jo, and B. K. Cho, J. Appl. Phys. **109** (2011) 07E109.
- [33] S. Ishida, M. Nakajima, H. Kito, Y. Tomioka, T. Ito, A. Iyo, H. Eisaki, and S. Uchida, Physica C **469** (2009) 905.
- [34] J. Hu and T. Rosenbaum, Nat. Mater. **7** (2008) 697.
- [35] K. K. Huynh, Y. Tanabe, K. Tanigaki, Phys. Rev. Lett. **106** (2011) 217004.
- [36] K. Wang, D. Graf, and C. Petrovic, Phys. Rev. B **87** (2013) 235101.
- [37] Y.-Y. Wang, Q.-H. Yu, and T.-L. Xia, Chin. Phys. B **25** (10) (2016) 107503.
- [38] K. Wang, D. Graf, H. Lei, S. W. Tozer, and C. Petrovic, Phys. Rev. B **84** (2011) 220401(R).
- [39] D. Bhoi, P. Mandal, P. Choudhury, S. Pandya, and V. Ganesan, Appl. Phys. Lett. **98** (2011) 172105.
- [40] A. A. Abrikosov, Phys. Rev. B **58** (1998) 2788.
- [41] B. Wu, V. Barrena, H. Suderow, and I. Guillaumón, Phys. Rev. Research **2** (2020) 022042(R).
- [42] R. D. H. Hinlopen, F. A. Hinlopen, J. Ayres, and N. E. Hussey, Phys. Rev. Research **4** (2022) 033195.
- [43] C. M. Hurd, *The Hall Effect in Metals and Alloys*, Plenum, New York, 1972.
- [44] N. P. Ong, Phys. Rev. B **43** (1991) 193.



# Supplementary information for “Electronic Transport and Fermi Surface Topology of Zintl phase Dirac

## Semimetal SrZn<sub>2</sub>Ge<sub>2</sub>”

M. K. Hooda<sup>1</sup>, A. Chakraborty<sup>1,2</sup>, S. Roy<sup>3</sup>, A. Agarwal<sup>1</sup>, P. Mandal<sup>4</sup>, S. N. Sarangi<sup>5</sup>, D. Samal<sup>5,6</sup>, V. P. S. Awana<sup>7</sup>,  
and Z. Hossain<sup>1</sup>

<sup>1</sup> Department of Physics, Indian Institute of Technology, Kanpur-208016, India

<sup>2</sup> Institute of Physics, Johannes Gutenberg Universität, Staudinger Weg 7, 55128 Mainz, Germany

<sup>3</sup> Vidyasagar Metropolitan College, 39, Sankar Ghosh Lane, Kolkata 700006, India

<sup>4</sup> Department of Condensed Matter and Material Physics, S. N. Bose National Centre for Basic Sciences, Block JD, Sector III, Salt Lake, Kolkata 700106, India

<sup>5</sup> Institute of Physics, Bhubaneswar, Bhubaneswar-751005, India

<sup>6</sup> Homi Bhabha National Institute, Anushakti Nagar, Mumbai 400085, India

<sup>7</sup> CSIR National Physical Laboratory, New Delhi, 110012, India

### 1. Calculation of topological indices

In order to validate the topological nature of the SrZn<sub>2</sub>Ge<sub>2</sub> and demonstrate the presence of nontrivial surface states, we have conducted thorough calculations of the topological indices associated with this system. It is important to emphasize that, despite the finite Fermi surface of the system, the conduction and valence sectors remain entirely separate. This separation is a crucial criterion for accurately determining the  $Z_2$  topological index within time reversal invariant systems. To provide a more detailed illustration, we have presented a magnified view near the crossing points, which is shown in Fig. S1. The  $Z_2$  topological number for bulk SrZn<sub>2</sub>Ge<sub>2</sub> can be determined by calculating the Wilson loop (Wannier charge center) for the six time-reversal invariant momentum (TRIM) plane. Below, we tabulate the  $Z_2$  numbers of the primitive unit cell for different TRIM planes in Table S1, which are calculated using the Wannier tools code [1]. The calculated topological indices yield the values of strong topological index:  $\mathbf{v}_0 = \text{mod}[(Z_2(k_i=0) + Z_2(k_i=0.5)), 2] = 1$  and weak topological indices:  $\mathbf{v}_i = Z_2(k_i=0.5) \Rightarrow \mathbf{v}_1=1, \mathbf{v}_2=1, \mathbf{v}_3=1$ , resulting in a  $Z_2$  topological number (1;111). These findings clearly demonstrate the strong topological character and nontrivial topology of SrZn<sub>2</sub>Ge<sub>2</sub>.

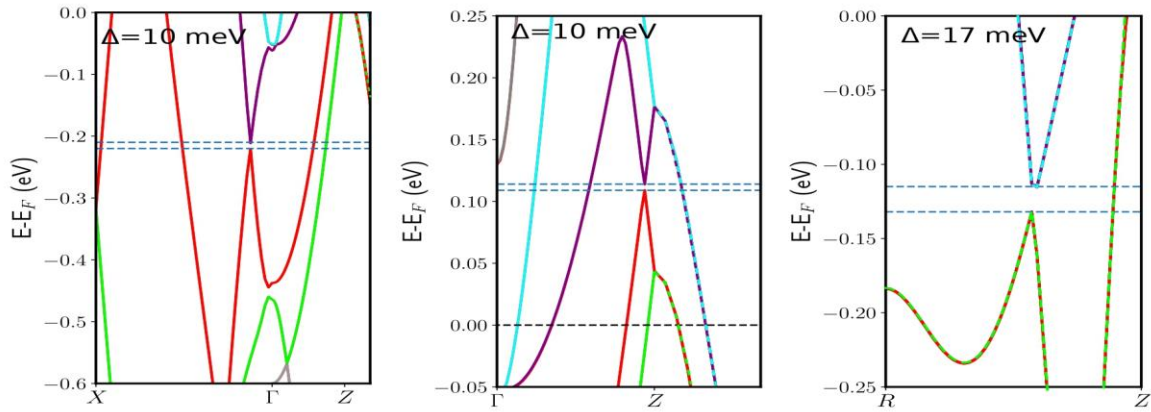


**Fig. S1.** The zoomed in view of different valence and conduction band crossing points along X-Γ-Z, Γ-Z and R-Z paths respectively. The gap values ( $\Delta$ ) are quoted for each plot. The calculated energy dispersion suggests that the valence and conduction sector possess a finite gap throughout the Brillouin zone.

| Table S1. $Z_2$ indices of SrZn <sub>2</sub> Ge <sub>2</sub> |           |             |                      |
|--|-----------|-------------|----------------------|
| Plane ( $i = x, y, z$ )                                      | $k_i = 0$ | $k_i = 0.5$ | $(v_0; v_1 v_2 v_3)$ |
| $Z_2$  | 0         | 1           | (1;111)              |

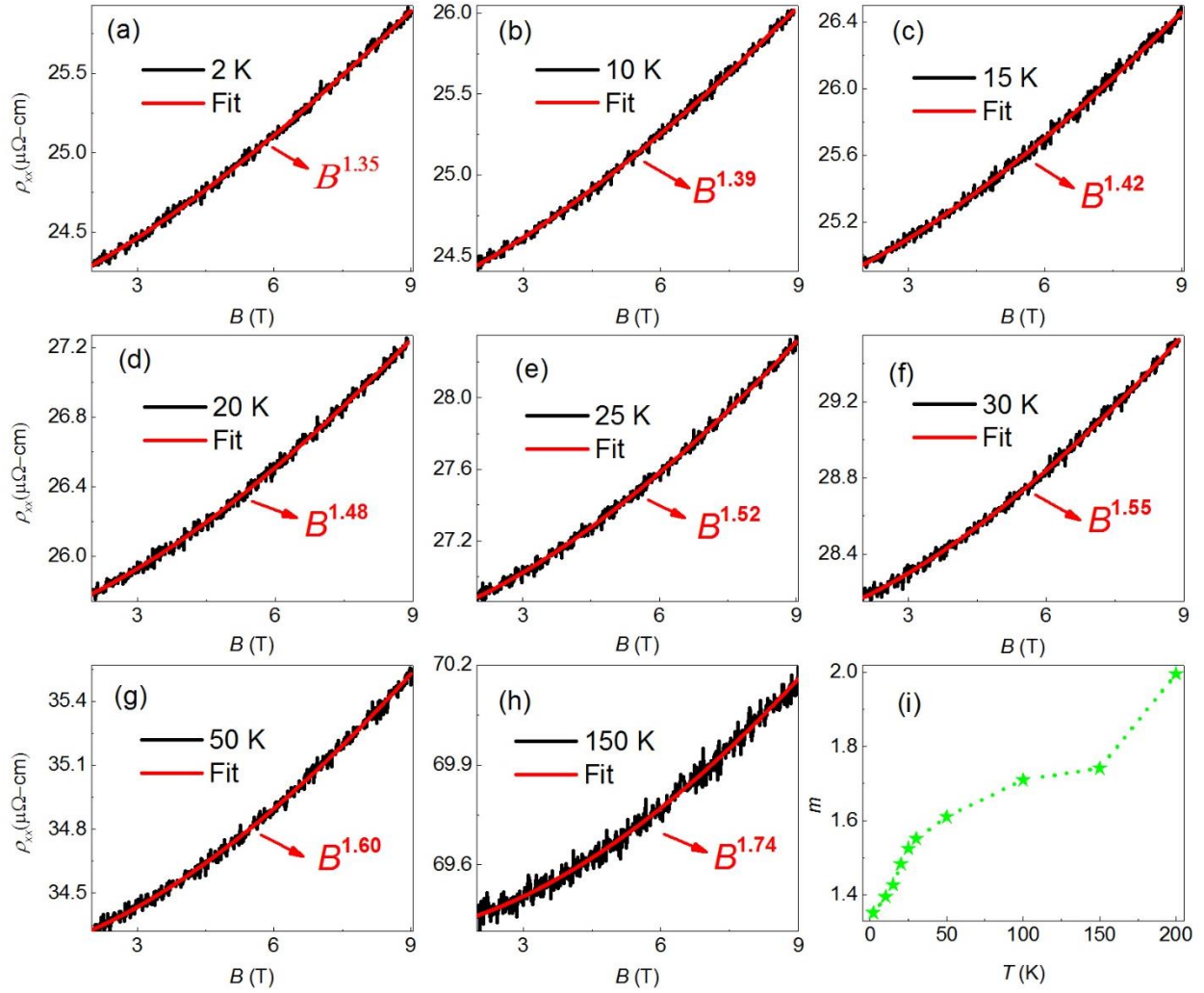


**Fig. S2.** The exponent  $m$  obtained from the power law ( $\text{MR} \propto B^m$ ) fit to the transverse MR data at various temperatures in the field range 2 to 9 T. The systematic decrease in  $m$  value with decreasing temperature indicates the predominance of linear component of MR at lower temperatures. At higher temperatures, linear component becomes weaker and quadratic component starts dominating. At  $T = 2$  K,  $m$  value is  $\sim 1.35$  for  $2 \leq B < 9$  T, which becomes  $\sim 1.09$  for fields above 5 T.

## 2. Linear magnetoresistance at low temperatures and high magnetic fields in $\text{SrZn}_2\text{Ge}_2$

Figure S2 (a-h) illustrates the field dependence of transverse magnetoresistance (MR) with a power law fit ( $\text{MR} \propto B^m$ ) in the field range of 2-9 T. The exponent  $m$ , obtained from the least-square fit, as a function of temperature, is presented in Fig. 2(i). For  $T \geq 200$  K, the exponent  $m$  value is 2. However, with decreasing temperature,  $m$  gradually decreases in a monotonic fashion, and tends to approach the linear behavior at very low temperatures, reaching  $\sim 1.35$  at 2 K. A similar power-law dependence has been observed in well-known topological semimetals like NbP and TaP [2,3]. Furthermore, at fields higher than 5 T,  $m$  reduces to  $\sim 1.09$  at 2 K (see the inset of Fig. 5(a) in the main text), indicating the presence of a dominant linear MR component, which coexists with a very small quadratic MR contribution. This kind of coexisting MR behavior is frequently reported in several topological semimetals [4-6]. Here, it is crucial to note that linear MR is not exhibited by all topological semimetals. For example,  $\text{MoGe}_2$  [7],  $\text{TaSb}_2$ ,  $\text{NbSb}_2$  [3],  $\text{TaSe}_3$  [8], and numerous others do not demonstrate linear MR.

Consequently, the observation of linear MR alone does not always serve as conclusive evidence for nontrivial topology. However, it can be considered as preliminary evidence for topological states, when other mechanisms contributing to linear MR, such as Hall field [9-12], charge/spin density waves [13], and open orbits [14], are eliminated. In the case of  $\text{SrZn}_2\text{Ge}_2$ , none of the aforementioned

mechanisms are present, allowing us to safely attribute the linear component of MR to the existence of Dirac states. Further evidence for the nontrivial topological character of SrZn<sub>2</sub>Ge<sub>2</sub> comes from our first principle calculations, which reveal the presence of Dirac cones and topological surface states intersecting the Fermi level, and contributing to the observed transport properties.

## References

- [1] Q. Wu, S. Zhang, H.-F. Song, M. Troyer, and A. A. Soluyanov, *Comput. Phys. Commun.* **224** (2018) 405.
- [2] C. Zhang, C. Guo, H. Lu, X. Zhang, Z. Yuan, Z. Lin, J. Wang, and S. Jia, *Phys. Rev. B* **92** (2015) 041203(R).
- [3] I. A. Leahy, Y.-P. Lin, P. E. Siegfried, A. C. Treglia, J. C. W. Song, R. M. Nandkishore, and M. Lee, *Proc. Natl. Acad. Sci. USA* **115** (42) (2018) 10570.
- [4] A. Wang, D. Graf, A. Stein, Y. Liu, W. Yin, and C. Petrovic, *Phys. Rev. B* **96** (2017) 195107.
- [5] H.-H. Kuo, J.-H. Chu, S. C. Riggs, L. Yu, P. L. McMahon, K. De Greve, Y. Yamamoto, J. G. Analytis, and I. R. Fisher, *Phys. Rev. B* **84** (2011) 054540.
- [6] K. Wang, D. Graf, H. Lei, S. W. Tozer, and C. Petrovic, *Phys. Rev. B* **84** (2011) 220401(R).
- [7] Y.-F. Huang, W.-L. Zhu, Y.-Y. Wang, Q.-X. Dong, L.-B. Zhang, C.-S. Li, H. OuYang, Z.-A. Ren, and G.-F. Chen, *Phys. Rev. B* **103** (2021) 134116.
- [8] G. Gatti, D. G.-Martínez, Q. S. Wu, J. Hu, S. N. Zhang, G. Autès, M. Puppín, D. Bugini, H. Berger, L. Moreschini, I. Vobornik, J. Fujii, J.-P. Ansermet, O. V. Yazyev, and A. Crepaldi, *Phys. Rev. B* **104** (2021) 155122.
- [9] C. Herring, *J. Appl. Phys.* **31** (1960) 1939.
- [10] M. Novak, S. Sasaki, K. Segawa, and Y. Ando, *Phys. Rev. B* **91** (2015) 041203(R).
- [11] M. M. Parish and P. B. Littlewood, *Nature* **426** (2003) 162.
- [12] J. Hu, M. M. Parish, and T. F. Rosenbaum, *Phys. Rev. B* **75** (2007) 214203.
- [13] Y. Feng, Y. Wang, D. M. Silevitch, J.-Q. Yan, R. Kobayashi, M. Hedo, T. Nakama, Y. Onuki, A. V. Suslov, B. Mihaila, P. B. Littlewood, and T. F. Rosenbaum, *Proc. Natl. Acad. Sci. USA* **116** (23) (2019) 11201.
- [14] B. Wu, V. Barrena, H. Suderow, and I. Guillaumon, *Phys. Rev. Research* **2** (2020) 022042(R).